Nano Res (2010) 3: 244–255
DOI 10.1007/s12274-010-1027-z
Research Article

Large Scale Photochemical Synthesis of M@TiO$_2$ Nanocomposites (M = Ag, Pd, Au, Pt) and Their Optical Properties, CO Oxidation Performance, and Antibacterial Effect

Shao Feng Chen[1,†], Jian Ping Li[2,†], Kun Qian[3], Wei Ping Xu[1], Yang Lu[1], Wei Xin Huang[3] and Shu Hong Yu[1] (✉)

[1] Division of Nanomaterials & Chemistry, Hefei National Laboratory for Physical Sciences at Microscale, Department of Chemistry, University of Science and Technology of China, Hefei 230026, China
[2] School of Pharmacy, Anhui University of Traditional Chinese Medicine, Hefei 230026, China
[3] Division of Chemical Physics, Hefei National Laboratory for Physical Sciences at Microscale, Department of Chemistry, University of Science and Technology of China, Hefei 230026, China

Received: 11 November 2009 / Revised: 12 January 2010 / Accepted: 28 January 2010
© The Author(s) 2010. This article is published with open access at Springerlink.com

ABSTRACT

Well-dispersed M@TiO$_2$ (M = Ag, Pd, Au, Pt) nanocomposite particles with a diameter of 200–400 nm can be synthesized on a large scale by a clean photochemical route which does not require any additives using spherical rutile nanoparticles as a support. The sizes of Pt, Au, and Pd nanoparticles formed on the surface of TiO$_2$ particles are about 1 nm, 5 nm, and 5 nm, respectively, and the diameter of Ag nanoparticles is in the range 2–20 nm. Moreover, the noble metal nanoparticles have good dispersity on the particles of the TiO$_2$ support, resulting in excellent catalytic activities. Complete conversion in catalytic CO oxidation is reached at temperatures as low as 333 and 363 K, respectively, for Pt@TiO$_2$ and Pd@TiO$_2$ catalysts. In addition, the antibacterial effects of the as-synthesized TiO$_2$ nanoparticles, silver nanoparticles, and Au@TiO$_2$ and Ag@TiO$_2$ nanocomposites have been tested against Gram-negative *Escherichia coli* (*E. coli*) bacteria. The results demonstrate that the presence of the TiO$_2$ matrix enhances the antibacterial effect of silver nanoparticles, and the growth of *E. coli* can be completely inhibited even if the concentration of Ag in Ag@TiO$_2$ nanocomposite is very low (10 μg/mL).

KEYWORDS

Nanocomposite, noble metals, CO oxidation, antibacterial

1. Introduction

Noble metals are widely used as catalysts but, due to their limited resources, how to use them more efficiently has become an emergent problem [1, 2]. Preparing ultrathin nanosized noble metal particles, especially with diameters less than 5 nm and even less than 1 nm, is an efficient way to increase their catalytic activity while reducing the amount of noble metal used [3]. Platinum serves as an excellent catalyst for a variety of applications, including CO/NO$_x$ oxidation, reforming syngas, and refining of petroleum [1]. Palladium is frequently used as a catalyst for CO oxidation and Suzuki reactions, in monometallic or bimetallic form [1, 4, 5]. Silver and gold nanoparticles can directly interact with some functional groups of

---

[†] These authors contributed equally to this work.
Address correspondence to shyu@ustc.edu.cn

many bacterial cell membranes, and thus have strong cytotoxicity to various bacterial cells at lower metal usage compared to that required for bulk metals [6, 7]. Organic frameworks [6, 7] and metal oxide supports [8–10] have frequently been used to maintain the dispersion of such noble metal nanoparticles. Due to their low price and ability to be prepared on a large scale, and since they are beneficial or, at worst, inert in processes catalyzed by noble metals, inorganic supports are preferred. TiO_2 is an active support for promoting the catalytic performance of Pt or Pd, as well as the antibacterial effects of Ag or Au [8, 11, 12]. On the other hand, TiO_2 is a typical semiconductor, widely used as photocatalyst for splitting water, decomposition of dyes, antibacterial applications under UV light, and so on [13–17].

To make the use of noble metals more economic and to improve their performance, it is crucial to control both the size of nanoparticles and their dispersity on a support [18–20]. Versatile colloidal methods for the synthesis of noble metal nanoparticles have emerged recently, but require the presence of organic molecules or solvents [21–23]. Generally, there are two methods to prepare a composite catalyst of such noble metal nanoparticles loaded on a support. One is a two-step method, involving the initial synthesis of noble metal nanoparticles, followed by a subsequent combination of these particles with a suitable support [24, 25]. The other method involves calcination of a mixed precursor of noble metal and support materials at relatively high temperature [26, 27]. However, aggregation of nanoparticles is hard to avoid in the first case, while the size of the noble metal particles is difficult to control in the second case [25, 28].

The photochemical route is a promising way to form noble metal–semiconductor nanocomposites *in situ* by reducing noble metal ions adsorbed on the surface of a semiconductor. It is well known that a semiconductor can be excited and then generate electrons (e^-) and holes (h^+) in the conduction band (CB) and valence band (VB) if the energy of the photons of the incident light is larger than that of the band gap of the semiconductor (Scheme 1) [13, 29]. However, previous work involving photocatalytic reduction of noble metal precursors was mostly aimed only at preparing nanoparticles, rather than nanocomposites for practical applications [30, 31]. Current methods of preparation of noble metal–support nanocomposites, as opposed to isolated metals [30], by photochemical routes need careful control of the reaction parameters and conditions, and amines and organic solvents are generally required in the synthesis mixture [32–34]. From the viewpoint of applications, any residue of amines or organic solvents on the noble metal loaded support will obviously affect the performance of the noble metal [35].

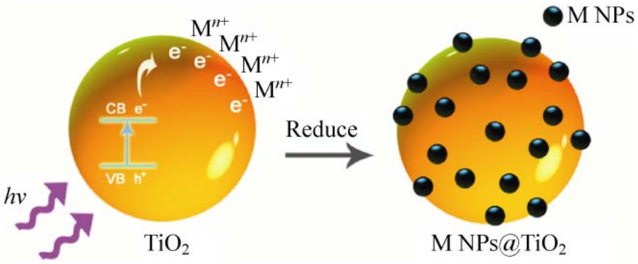

Scheme 1 Photochemical route for formation of M@TiO_2 nanocomposites. CB: conduction band; VB: valence band; M: Ag, Pd, Au, Pt; e^-: photoexcited electrons; h^+: photoexcited holes; NPs: nanoparticles

In this paper, we report an efficient method for the synthesis of a series of well-dispersed M@TiO_2 (M = Ag, Pd, Au, Pt) nanocomposite particles with a diameter of 200–400 nm on a large scale by a clean photochemical route without any additives being required and using spherical rutile nanoparticles as support. The catalytic CO oxidation performance and antibacterial effects of the products have been investigated.

2. Experimental

2.1 Materials

$TiCl_3$ (M_w = 154.23, solution in 15 wt%–20 wt% dilute aqueous hydrochloric acid), chitosan (degree of deacetylation > 90%), $AgNO_3$ (M_w = 169.87), $HAuCl_4$ (M_w = 339.79), acetic acid (M_w = 60.06), hydrazine (M_w = 50.06, 85%*v*/*v*), and acetone (M_w = 58.08) were analytical grade from Shanghai Chemical Reagents Corporation (SCRC). Ultrapure water was prepared using a Millipore Simplicity UV system.

2.2 Synthesis of rutile TiO_2

5 grams of chitosan powder was poured into a vessel containing 100 mL of deionized water and 5 mL of acetic acid. The mixture was stirred for 6 h at 90 °C, and finally cooled naturally to room temperature. 10 grams of this as-synthesized chitosan solution was added dropwise into a vessel containing 40 mL of acetone and 4 mL of $TiCl_3$ solution, and then the vessel was covered with parafilm and left at room temperature for 2 weeks. The resulting white deposit was immersed in water to dissolve the chitosan, and then the suspension was centrifuged and washed several times with deionized water and ethanol. Finally, the powder was dried at 60 °C.

2.3 Synthesis of M@TiO_2 nanohybrid materials by photoreduction

50 mg of as-synthesized TiO_2 powder and 1 mL (5 mol/L $AgNO_3$, or 2.5 mmol/L $HAuCl_4$), or 3 mL (2.5 mmol/L $PdCl_2$, or 2.5 mmol/L H_2PtCl_6) of an aqueous metal salt solution were dispersed with 100 mL of deionized water in a Pyrex flask with capacity of about 250 mL under stirring. The flask was exposed to light from a high-pressure Xe lamp (150 W, PerkinElmer Co.). The reaction was carried for 25 min ($AgNO_3$) or 1.5 h ($PdCl_2$, $HAuCl_4$, H_2PtCl_6). Then the powder was collected by centrifugation and washed twice by deionizedwater and ethanol. Finally, the resulting powder was dried at 60 °C.

2.4 Catalytic oxidation of CO

The catalytic activity was evaluated with a fixed-bed flow reactor. The weight of catalyst used was 48.5 mg, and the reaction gas consisting of 1%(*v*/*v*) CO and 99%(*v*/*v*) dry air was fed at a rate of 20 mL/min. The composition of the effluent gas was detected with an online GC-14C gas chromatograph. The conversion of CO was calculated from the difference in CO concentrations between the inlet and outlet gases.

2.5 Antibacterial applications

To examine the susceptibility of Gram-negative *Escherichia coli (E. coli)* to different hybrid nanoparticles, agar plates were employed. Bacterial solution (100 μL) cultured in *Luria-Bertani* (LB) liquid medium with a concentration of 10^5 cfu/mL of *E. coli* was plated on agar plates with 20 μg/mL of Au@TiO_2 or Ag@TiO_2 (cfu: colony-forming units).

The detailed antibacterial effects of as-synthesized materials were assessed by culturing *E. coli* at 37 °C in a shaking incubator at 280 rpm (in 50 mL LB broth medium supplemented with 10^7 cfu/mL bacterial solution and different concentrations of as-synthesized materials). *E. coli* inoculum was prepared by culture overnight at 35 °C and 200 rpm in 50 mL LB broth medium from a single colony surface on LB agar plates, and then about 2 mL of the culture was transferred into 100 mL of fresh LB medium and further conditioned at 35 °C and 200 rpm to prepare the inoculum. For each growth inhibtion experiment, 5 mL of *E. coli* inoculum was added to 50 mL of fresh LB broth medium containing as-synthesized nanoparticles with different concentrations, i.e., 0.5–10 μg/mL. For Ag nanoparticles or Au@TiO_2, the concentrations given in Fig. 8 and the main text refer to the concentration of the metal. The experiments were performed three times. The optical density at 600 nm was measured at hourly intervals by UV/vis spectrophotometry.

2.6 Characterization

Surface charges (zeta potentials) and particle sizes of each sample were measured on a Nano-ZS Zetasizer dynamic light scattering detector (Malvern Instruments, UK) equipped with a 4.0 mW internal laser. X-ray powder diffraction patterns were collected on a Philips X'Pert Pro Super Diffractometer using Cu Kα radiation (λ = 1.541 874 Å). A Thermo-VG Scientific ESCALAB 250 instrument was used for X-ray photoelectron spectroscopy (XPS) measurements. UV/vis spectra were recorded with a Shimadzu UV-240 spectrophotometer. Fourier transform infrared (FTIR) and Raman spectra were measured using Magna IR-750 (Nicolet Instrument Co. USA) and Ramanlog (Spex, USA) spectrometers, respectively. The photoluminescence spectra measurements were conducted on a Fluorolog3-TAU-P instrument. Transmission electron microscope (TEM) images were obtained using a JEOL JEM 2011 microscope with an accelerating voltage of 200 kV. Scanning electron microscope (SEM) measurements were carried out using a Zeiss Supra 40 microscope. Two-photon images were recorded using a Zeiss LSM510 instrument. Nitrogen sorption data were obtained with a Micromeritics TriStar 3000 automated gas adsorption analyzer. Surface areas were obtained using the Brunauer–Emmet–Teller (BET) method.

3. Results and discussion

3.1 Synthesis of rutile TiO_2 nanostructures

Hydrolysis and subsequent oxidation by dissolved oxygen of Ti(Ⅲ) species are slow at room temperature in an acetone/water mixed solvent containing chitosan [36, 37]. After removing the chitosan by extraction with deionized water, the resulting white powder was collected by centrifugation. FTIR spectra indicate that no chitosan residue remains in the powder and a relatively strong peak at 1630 cm^{-1} can be attributed to hydroxyl groups (see Fig. S-1 in the Electronic Supplementary Material (ESM)). The X-ray photoelectron (XPS) spectra of the powder show the binding energies of Ti $2p_{1/2}$ and Ti $2p_{3/2}$ are 464.4 and 458.69 eV, respectively, confirming that no Ti(Ⅲ) species remain in the sample (see Fig. S-2 in the ESM).

The X-ray diffraction (XRD) pattern in Fig. 1(a) shows that the as-synthesized powder is the rutile phase of TiO_2. Calculations based on the half-widths of the (110), (101), and (111) diffraction peaks using the Scherrer formula indicated that the average size of the crystallites was about 10 nm. The symmetry of rutile TiO_2 is tetragonal $P4_2/mnm$, in which the titanium atoms (gray) occupy the corners and the body center, and oxygen atoms (red) occupy ± (0.3, 0.3, 0) and ± (0.8, 0.2, 0.5) sites as shown in Fig. 2(d).

Figure 1(b) shows the Raman-active fundamental modes of the as-obtained TiO_2. The A_{1g} (603 cm^{-1}) and E_g (432 cm^{-1}) modes as well as a second-order peak at about 240 cm^{-1} are the dominant peaks and characteristic of the rutile phase of TiO_2. The Raman peak at about 105 cm^{-1} and a broad band at about 685 cm^{-1} are due to a size effect and indicate that the size of the particles is less than 10 nm [38]. SEM images show that uniform spheres with a diameter of 200–400 nm can be obtained on a large scale (see Fig. S-3 in the ESM). The small size of the TiO_2 particles means a high surface-to-volume ratio. The BET surface area of the powder is 173 m^2/g (Fig. 3).

The high-magnification TEM images in Figs. 2(a) and 2(b) show that the spherical aggregates have good crystallinity and are composed of nanoparticles with a diameter less than 10 nm, consistent with the Raman spectra and the XRD data discussed above. A high-resolution TEM (HRTEM) image (Fig. 2(c)) shows that the lattice fringes on the crystal face have a spacing of 3.28 Å, corresponding to the (110) face of rutile TiO_2. The (110) surface obtained by cleaving a

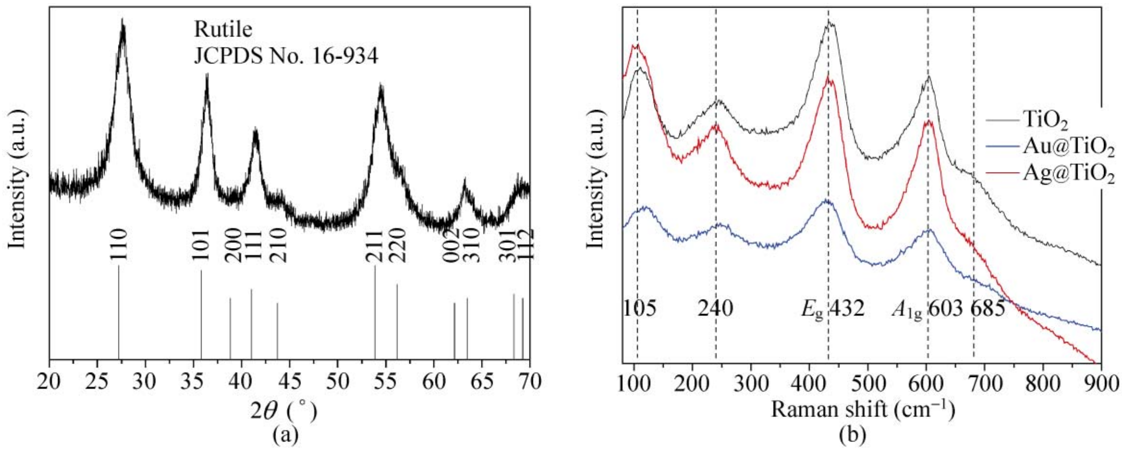

Figure 1 (a) XRD pattern of as-synthesized rutile TiO_2 and standard reference pattern (JCPDS No. 16-934); (b) Raman spectra of as-synthesized rutile TiO_2, Au@TiO_2, and Ag@TiO_2

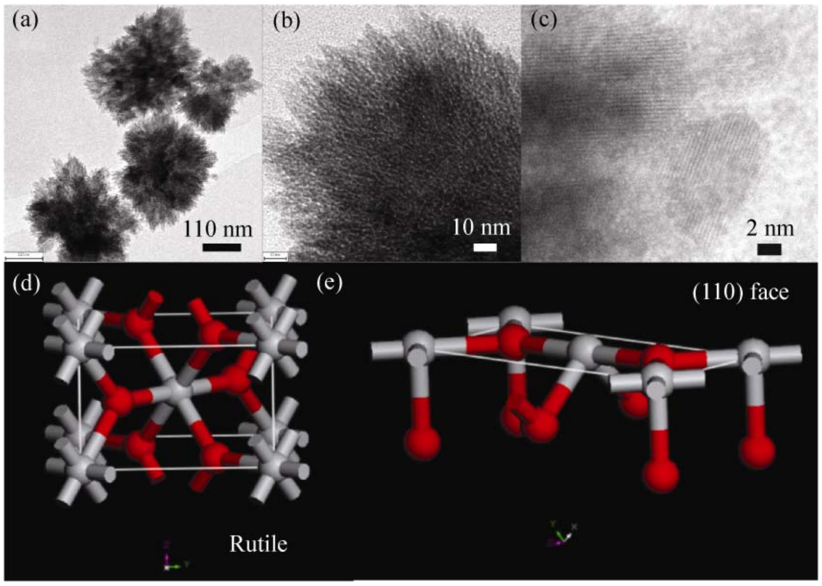

Figure 2 (a), (b) TEM, and (c) high-resolution TEM (HRTEM) images of as-synthesized rutile TiO_2. (d) Atomic cell model of rutile TiO_2, and (e) (110) surface of rutile TiO_2 (where the gray balls and red balls represent Ti and O atoms, respectively) obtained using Accelrys *Materials Studio Modeling* 3.1

rutile unit cell is a Ti-rich plane, which indicates that it has a positive charge. The exposed titanium atoms on the plane are readily coordinated by hydroxyl groups as shown in the FTIR spectrum (see Fig. S-1 in the ESM). Moreover, the positively charged plane leads to the TiO_2 colloids having a high zeta potential (45.8 mV), indicating a good stability in solution.

3.2 Synthesis of M@TiO_2 hybrid materials by photoreduction

After irradiation by a Xe light source, the white suspension of TiO_2 and an appropriate metallic precursor became light yellow–green (Ag), dark (Pd), purple (Au), and yellowish (Pt), as shown in Fig. 4. Comparison of the bright field images and two-photon images of the powders showed no obvious signal intensity increase in the case of pure TiO_2. Two-photon signals only arise from the surface plasmon resonance (SPR) effect of noble metal nanoparticles [39] (see Fig. S-4 in the ESM) and the images of noble metal containing powders after the photoreduction process showed typical two-photon effects and good co-localization with the bright field images, which indicates that the noble metal must be deposited on the TiO_2 nanoparticles with no noble metal nanoparticles being localized outside the TiO_2 matrix (see Fig. S-4 in the ESM). Furthermore, the XPS spectra of the four M@TiO_2 samples (M = Ag, Pd, Au, Pt) all confirm the presence of the noble metals in their elemental states (see Fig. S-5 in the ESM). It is believed that photogenerated electrons from the conduction band are responsible for the reduction of metallic ions adsorbed on the surface of TiO_2 nanoparticles (Scheme 1) [30]. Inductively coupled plasma atomic emission spectrometry (ICP-AES) of the solution obtained after centrifugation of the reaction suspension indicated an almost total absence of noble metal ions, which means that all the noble metal ions were deposited on the TiO_2.

3.3 Catalytic performance of Pt@TiO_2 and Pd@TiO_2 in the CO oxidation reaction

The loadings (weight ratio of metal to TiO_2 support) of Pt and Pd in the catalysts were 2.9 wt% and 1.5 wt%, respectively, as given by ICP-AES. The TEM images of Pt@TiO_2 and Pd@TiO_2 nanocomposites given in Fig. 5 show that metal nanoparticles are decorated

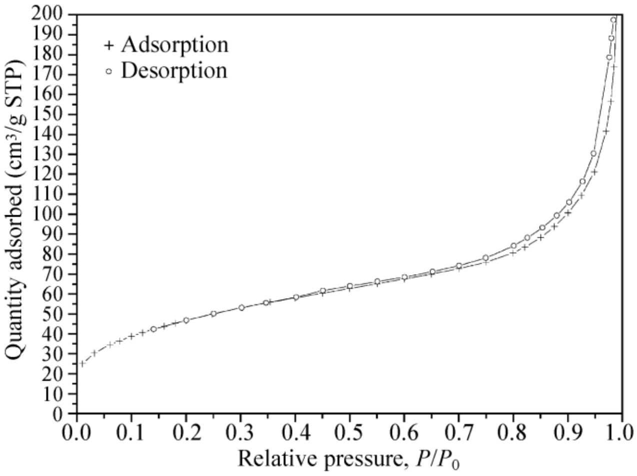

Figure 3 BET adsorption-desorption isotherms of the as-synthesized rutile TiO_2 powder

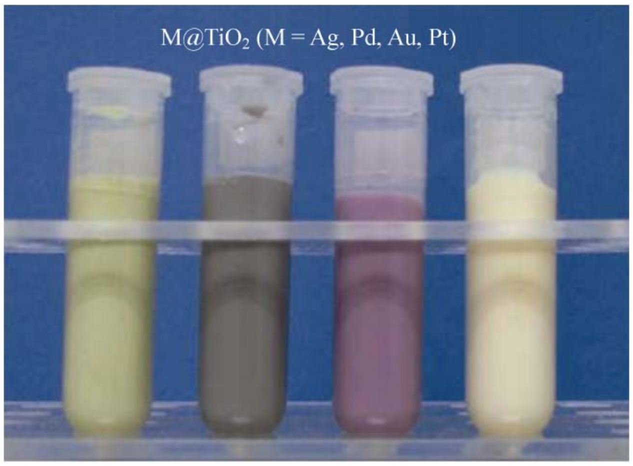

Figure 4 Photographs of suspensions of (from left to right) Ag@TiO$_2$, Pd@TiO$_2$, Au@TiO$_2$, and Pt@TiO$_2$

homogeneously on TiO$_2$ particles. The sizes of Pt and Pd nanoparticles are about 1 nm (Figs. 5(a) and 5(b)) and 5 nm (Figs. 5(c) and 5(d)), respectively. These should have good catalytic activity for CO oxidation, given the well-known activity-size relation [18–20]. The energy dispersive spectra (EDS) show the presence of Pt and Pd elements in the respective samples (see Figs. S-6 and S-7 in the ESM). As-prepared Pt@TiO$_2$ particles show good catalytic activity for CO oxidation (Fig. 6(a)). On the third pass through the reactor containing Pt@TiO$_2$, CO conversion reached 100% at 333 K. It is well known that Pt-loaded metal oxide supported catalysts are generally not efficient at low ratios of O$_2$/CO or temperatures below 443 K, because CO and O$_2$ are adsorbed at similar sites, and strong CO adsorption hinders O$_2$ adsorption on the noble metal catalyst [40–42]. In our case, the high conversion obtained at low temperature indicates the high activity of the small nanoparticles with a large number of Pt atoms with low coordination number present on the surface of nanoparticles with a diameter of 1 nm [19, 20, 43]. The Pt and Pd nanoparticles shown in Fig. 5 are too unstable to give a high-magnification TEM image, because they melt under the electron beam of a TEM. For Pd@TiO$_2$, CO conversion reached 100% at 363 K (Fig. 6(b)). Complete conversion at this low temperature can also be attributed to the small size of Pd nanoparticles. However, its catalytic activity was lower in the second pass through the reactor, which could be due to melting of the nanoparticles or further growth of unstable Pd nanoparticles [4, 44].

3.4 Antibacterial effect of Ag@TiO$_2$ and Au@TiO$_2$ nanocomposites

Figure 7 shows TEM and HRTEM images of Ag@TiO$_2$ and Au@TiO$_2$ nanocomposites. The size distribution of Ag ranges from 2 to 20 nm (Figs. 7(a) and 7(b)). The lattice fringe spacing for Ag@TiO$_2$ is 2.36 Å, which is consistent with the [111] spacing of Ag (Fig. 7(c)). The Au nanoparticles with a diameter of about 5 nm are monodisperse on the surface of TiO$_2$ support as shown in Figs. 7(d) and 7(e). The lattice fringe spacing is

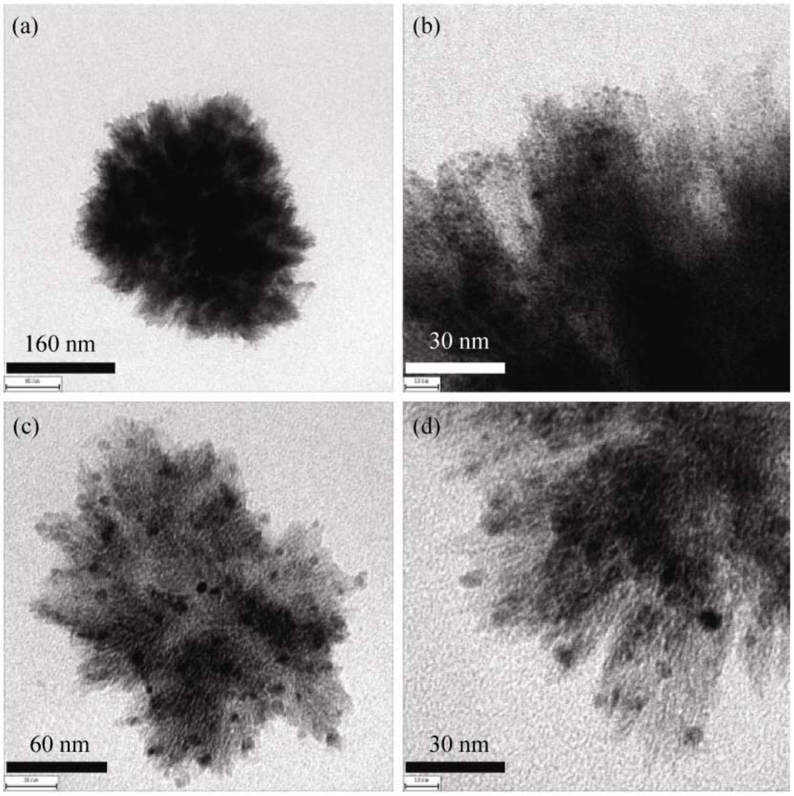

Figure 5 TEM images of the M@TiO$_2$ nanocomposites: (a) and (b) Pt@TiO$_2$; (c) and (d) Pd@TiO$_2$

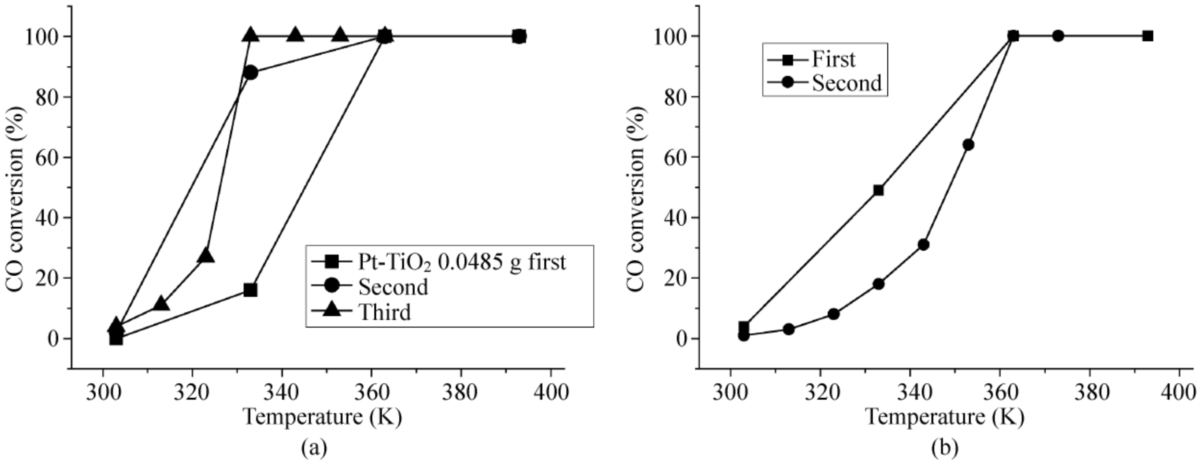

Figure 6 Catalytic performance of the nanocomposites (a) Pt@TiO_2 and (b) Pd@TiO_2. The weight of catalyst was 48.5 mg. The reaction gas consisted of 1% CO and 99% dry air, and was fed at a rate of 20 mL/min

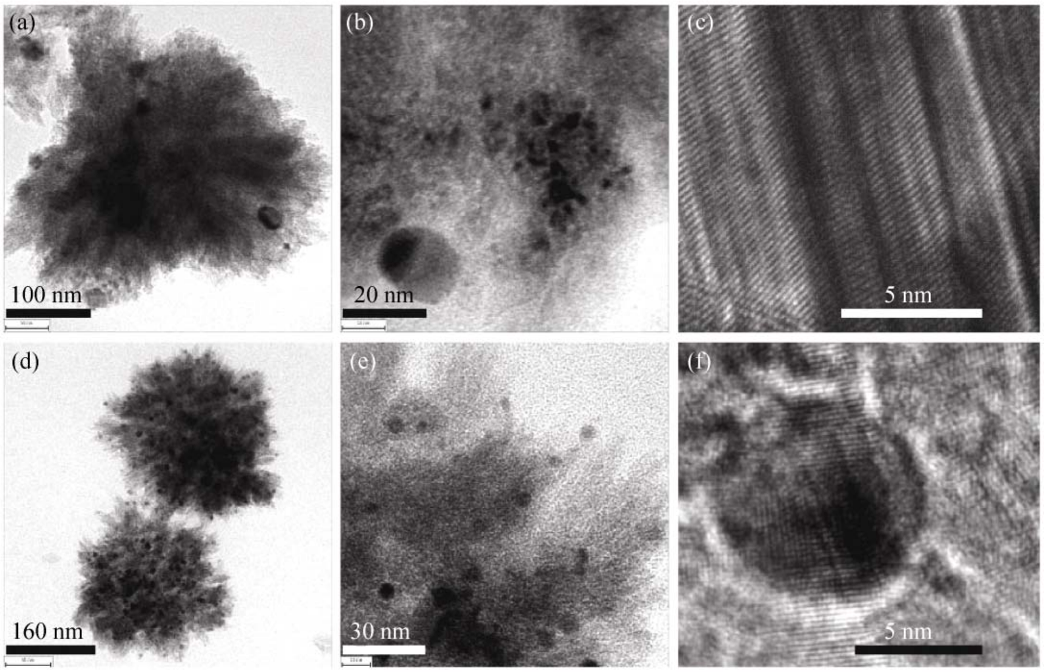

Figure 7 TEM and HRTEM images: (a)–(c) Ag@TiO_2, and (d)–(f) Au@TiO_2. The lattice fringe spacing in (c) is 2.36 Å, corresponding to the [111] direction of Ag (JCPDS Card No. 89-3722); the lattice fringe spacing in (f) is 2.04 Å, corresponding to the [200] direction of Au (JCPDS Card No. 4-784)

2.04 Å, which corresponds to the (200) plane of Au (Fig. 7(f)). The EDS show the presence of Au and Ag elements in the samples, respectively (see Figs. S-8 and S-9 in the ESM). The XPS spectra of the Ag@TiO_2 composites show peaks at 367.4 and 373.5 eV which can be attributed to Ag $3d_{5/2}$ and Ag $3d_{3/2}$ of elemental Ag, respectively [45] (see Fig. S-5 in the ESM). ICP-AES indicates that the loadings of Ag and Au in Ag@TiO_2 and Au@TiO_2 are about 1.08 wt% and 0.99 wt%, respectively. The small size of the metal nanoparticles should lead to high antibacterial activity.

A visual antibacterial test against *E. coli* was used to compare colonies on agar plates in the presence or absence of the hybrid nanomaterials. Approximately 10^4 colony-forming units (cfu) of *E. coli* were cultured on LB agar plates as control, and LB agar plates supplemented with 20 μg/mL Ag@TiO_2 and Au@TiO_2 particles. After incubation at 37 °C for 24 h, bacterial colony crowding was observed on the control plates in the absence of any additives (see Fig. S-10 in the ESM). The presence of the Au@TiO_2 nanocomposite inhibited bacterial growth by approximately 80%, indicating that it has a good antibacterial effect (the purple plate in the insert in Fig. 8(b)). The smooth yellow plate containing Ag@TiO_2 nanoparticles (the insert in Fig. 8(c)) displays nearly complete inhibition of bacterial growth, which shows the excellent antibacterial effect of Ag nanoparticles when loaded on TiO_2 particles.

A detailed investigation of the dynamics of bacterial growth was carried out by measuring the optical density (O.D.) of the LB broth medium by UV/vis spectrophotometry [6]. Plots of normalized O.D. [(cfu/mL)/(cfu/mL)] as a function of time are shown in Fig. 8. Addition of TiO_2 with different concentrations of 0.5, 1, and 5 μg/mL results in no significant inhibition of bacterial growth (Fig. 8(a)) compared with that in the control experiment without any added TiO_2. In contrast, adding the Au@TiO_2 nanocomposite with concentrations of 1, 2, 5, and 10 μg/mL has a notable antibacterial effect (Fig. 8(b)), and increasing the concentration of Au@TiO_2 leads to increasing inhibition of bacterial growth.

An excellent antibacterial effect can be achieved in the case of the Ag@TiO_2 nanocomposite (Fig. 8(c)). When the concentration of the nanocomposite was 10 μg/mL, the growth of *E. coli* was completely

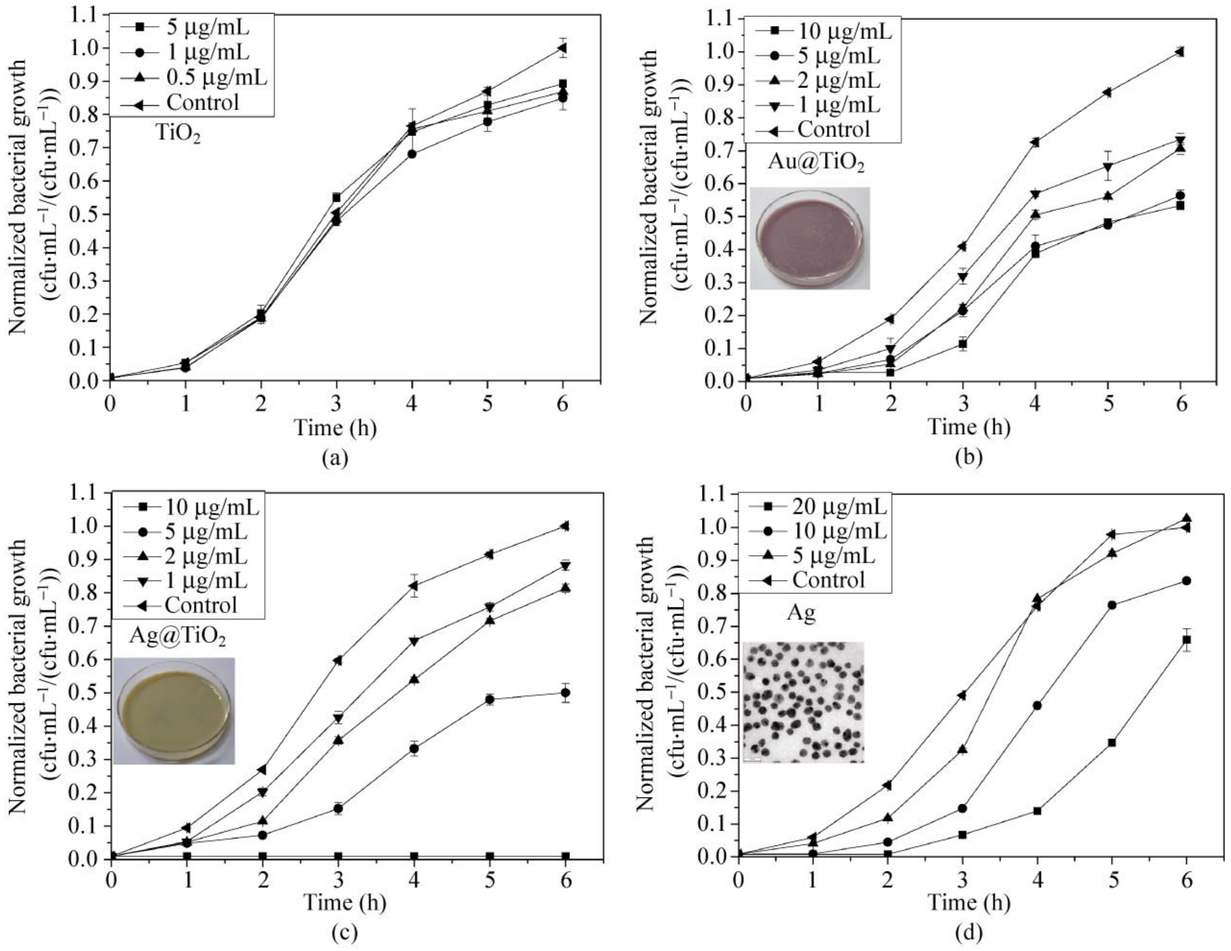

Figure 8 Curves showing the antibacterial effects as a function of time of (a) pure TiO_2, (b) Au@TiO_2, (c) Ag@TiO_2, and (d) pure silver nanoparticles with a diameter of 30–50 nm. Photographs inserted in (b) and (c) show petri dishes supplemented with Au@TiO_2 (b) and Ag@TiO_2 (c) at a loading of 20 μg/mL dispersed in medium with 100 μL of 105 cfu/mL *E. coli*

inhibited, which is similar to what was observed in the LB agar plate (the insert in Fig. 8(c)). It has previously been found [8, 9, 46, 47] that silver-doped titania has better antibacterial effect than pure silver particles, only when the loading is very high, about 5–70 times more than we used here. In fact, lowering the concentration of the nanocomposite to 5 μg/mL, also has a significant effect on bacterial growth. Although the detailed mechanism of the antibacterial effect of silver nanoparticles is still unclear, there are some clues in the literature. Silver nanoparticles can interact with sulfur-containing proteins from cell membrane and phosphorus-containing compounds in cells, attacking the respiratory chain, with cell division leading to cell death [48, 49]. For a given dosage of silver, smaller particle sizes mean a larger number of particles, which increases the contact between the bacterial cell membrane and the silver nanoparticles. A control experiment (Fig. 8(d)) shows the antibacterial effect of pure silver nanoparticles synthesized by a previous microwave method [50]. The silver nanoparticles, with diameters of 30–50 nm, cannot completely depress the bacterial growth even when the silver concentration reached 20 μg/mL. It is observed that the nanoparticles aggregated together and sedimented during the shaking process, decreasing the possibility of interaction of the bacterial cells with the silver nanoparticles.

Small silver nanoparticles, with a diameter less than 10 nm, give rise to electronic effects which enhance their surface reactivity. In our case, the tiny Ag or Au nanoparticles are loaded on monodisperse rutile nanospheres, preventing their aggregation and protecting their high surface activity. Furthermore, the zeta potentials of Au@TiO_2 and Ag@TiO_2 are positive, +29.8 and +33.2 mV, respectively. It is well known that the charge on the membrane of *E. coli* is negative. Hence, electrical attraction between the bacteria and as-synthesized hybrid materials increases their collision possibility and results in the metal nanoparticles being highly efficient inhibitors of bacterial growth.

3.5 Photoluminescence of TiO_2, Ag@TiO_2, and Au@TiO_2

The photoreduction process and deposition of metal nanoparticles have no obvious effect on the Raman spectrum of the TiO_2 matrix (Fig. 1(b)). In their UV/vis spectra, the as-synthesized TiO_2 and metal@TiO_2 materials all have strong absorbance around 300 nm and broad photoabsorption region in the visible region (400–800 nm) [16, 51] (see Fig. S-11 in the ESM). No typical absorbance peaks of nanosized silver and gold are observed, which is similar to a previous report for materials with such a low metal concentration [51]. Photoluminescence (PL) bands of TiO_2 and metal@TiO_2 hybrid materials are located in the violet region (Fig. 9). The observed narrow emission band is in contrast to the broad emission band reported previously when the size of TiO_2 particles was very small [52]. When as-synthesized TiO_2 nanoparticles were excited at 366 nm (Fig. 9(b)), the maximum

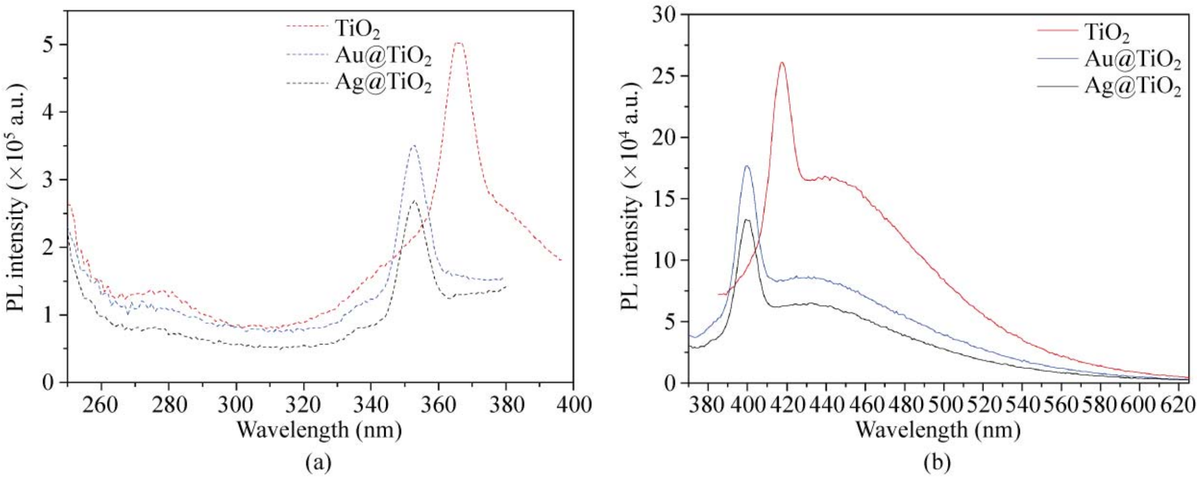

Figure 9 Photoluminescence spectra of as-synthesized TiO_2, Ag@TiO_2, and Au@TiO_2: (a) excitation spectra; (b) emission spectra

emission occured at 417 nm (2.97 eV), which arises from free excitons and is near to the bandgap of bulk rutile (3.0 eV) [53]. A large shoulder band around 450 nm (2.76 eV) shown in Fig. 9(b) can be ascribed to oxygen vacancies or a defect state in the nanostructure [53]. During the irradiation process, the *in situ* absorbance and reduction of the metallic precursor on the surface change the defect state of TiO_2. Hence, the maximum excitation and emission bands of the Ag@TiO_2 or Au@TiO_2 show a small blue-shift compared with TiO_2, with emission peaks observed at 400 nm (3.10 eV) for Au@TiO_2 and 399 nm (3.11 eV) for Ag@TiO_2 when excited at 352 nm. The introduction of nanosized metal nanoparticles on TiO_2 leads to quenching of the PL intensity, but the emission bands remain narrow [51]. The narrow emission bands of the nanocomposites may enable them to act as selective optical windows for some special applications.

4. Conclusions

A general photochemical route to synthesize Ag@TiO_2, Pd@TiO_2, Au@TiO_2, and Pt@TiO_2 nanocomposites on a large scale has been devised. Four kinds of metal (Ag, Pd, Au, Pt) precursors can be reduced to uniform nanoparticles in a clean way when the solution is irradiated by a Xe light source, and are deposited on the TiO_2 matrix to form metal–TiO_2 nanocomposite particles without requiring the introduction of any toxic agents. The nanocomposites synthesized at room temperature contain rutile TiO_2 particles with a size of 200–400 nm and ultra small metal nanoparticles with diameters of less than 10 nm. The Pt@TiO_2 nanocomposite exhibits good activity for CO catalytic oxidation with conversion temperatures as low as 333 K. Antibacterial experiments demonstrated that 20 μg/mL of Au@TiO_2 has an obvious antibacterial effect, while a dosage of as low as 10 μg/mL of as-synthesized Ag@TiO_2 nanocomposite shows excellent antibacterial capability, because the electrical attraction between negative *E. coli* and the nanocomposite with its high positive charge promotes the interaction between bacterial cells and silver nanoparticles. These nanocomposites synthesized by this clean photochemical route without requiring any additives are expected to find potential applications as catalysts, antibacterial agents and in other fields.

Acknowledgements

S. -H. Yu acknowledges the funding support from the National Basic Research Program of China (No. 2010CB934700), the Program of International S & T Cooperation (No. 2010GR0314), the National Science Foundation of China (NSFC) (Nos. 50732006, 20671085), and the Partner-Group of the Chinese Academy of Sciences & the Max Planck Society. S. F. Chen thanks the Innovation Fund for Graduate Students of USTC (2006) for support.

Electronic Supplementary Material: Two-photon images, FTIR spectra, EDS, UV/vis spectra, and SEM images are available in the online version of this article at http://dx.doi.org/10.1007/s12274-010-1027-z and are accessible free of charge.

Open Access: This article is distributed under the terms of the Creative Commons Attribution Noncommercial License which permits any noncommercial use, distribution, and reproduction in any medium, provided the original author(s) and source are credited.

References

[1] Ertl, G. *Handbook of Heterogeneous Catalysis;* Wiley-VCH: Weinheim, 2008.

[2] Huang, S. Y.; Ganesan, P.; Park, S.; Popov B. N. Development of a titanium dioxide-supported platinum catalyst with ultrahigh stability for polymer electrolyte membrane fuel cell applications. *J. Am. Chem. Soc.* **2009**, *131*, 13898–13899.

[3] Chen, J.; Lim B.; Lee, E. P.; Xia, Y. Shape-controlled synthesis of platinum nanocrystals for catalytic and electrocatalytic applications. *Nano Today* **2009**, *4*, 81–95.

[4] Kaya, S.; Üner, D. CO oxidation over mono and bi-metallic sequentially impregnated Pd–Pt catalysts. *Turk. J. Chem.* **2008**, *32*, 645–652.

[5] Miyaura, N.; Suzuki, A. Palladium-catalyzed cross-coupling reactions of organoboron compounds. *Chem. Rev.* **1995**, *95*, 2457–2483.

[6] Sondi, I.; Salopek-Sondi, B. Silver nanoparticles as antimicrobial agent: A case study on *E. coli* as a model for Gram-negative bacteria. *J. Colloid Interface Sci.* **2004**, *275*, 177–182.

[7] Zhang, Y. W.; Peng, H. S.; Huang, W.; Zhou, Y. F.; Yan, D. Y. Facile preparation and characterization of highly

antimicrobial colloid Ag or Au nanoparticles. *J. Colloid Interface Sci.* **2008**, *325*, 371–376.

[8] Thiel, J.; Pakstis, L.; Buzby, S.; Raffi, M.; Ni, C.; Pochan, D. J.; Shah, S. I. Antibacterial properties of silver-doped titania. *Small* **2007**, *3*, 799–803.

[9] Gunawan, C.; Teoh, W. Y.; Marquis, C. P.; Lifia, J.; Amal, R. Reversible antimicrobial photoswitching in nanosilver. *Small* **2009**, *5*, 341–344.

[10] Kim, Y. H.; Kim, C. W.; Cha, H. G.; Lee, D. K.; Jo, B. K.; Ahn, G. W.; Hong, E. S.; Kim, J. C.; Kang, Y. S. Bulklike thermal behavior of antibacterial Ag–SiO_2 nanocomposites. *J. Phys. Chem. C* **2009**, *113*, 5105–5110.

[11] Epling, W. S.; Cheekatamarla, P. K.; Lane, A. M. Reaction and surface characterization studies of titania-supported Co, Pt and Co/Pt catalysts for the selective oxidation of CO in H_2-containing streams. *Chem. Eng. J.* **2003**, *93*, 61–68.

[12] Keleher, J.; Bashant, J.; Heldt, N.; Johnson, L.; Keleher, J.; Bashant, J.; Heldt, N.; Johnson, L.; Li, Y. Photo-catalytic preparation of silver-coated TiO_2 particles for antibacterial applications. *World J. Microbiol. Biotechnol.* **2002**, *18*, 133–139.

[13] Kudo, A.; Miseki, Y. Heterogeneous photocatalyst materials for water splitting. *Chem. Soc. Rev.* **2009**, *38*, 253–278.

[14] Liu, S. J.; Wu, X. X.; Hu, B.; Gong, J. Y.; Yu, S. H. Novel anatase TiO_2 boxes and tree-like structures assembled by hollow tubes: *D,L*-malic acid-assisted hydrothermal synthesis, growth mechanism, and photocatalytic properties. *Cryst. Growth Des.* **2009**, *9*, 1511–1518.

[15] Chen, W. J.; Tsai, P. J.; Chen, Y. C. Functional Fe_3O_4/TiO_2 core/shell magnetic nanoparticles as photokilling agents for pathogenic bacteria. *Small* **2008**, *4*, 485–491.

[16] Chen, X. B.; Mao, S. S. Titanium dioxide nanomaterials: Synthesis, properties, modifications, and applications. *Chem. Rev.* **2007**, *107*, 2891–2959.

[17] Thompson, T. L.; Yates, J. T. Surface science studies of the photoactivation of TiO_2—New photochemical processes. *Chem. Rev.* **2006**, *106*, 4428–4453.

[18] Haruta, H.; Yamada, M.; Kobayashi, T.; Iijima, S. Gold catalysts prepared by coprecipitation for low-temperature oxidation of hydrogen and of carbon monoxide. *J. Catal.* **1989**, *115*, 301–309.

[19] Haruta, M. Copper, silver and gold in catalysis—Preface. *Catal. Today* **1997**, *36*, 1.

[20] Valden, M.; Lai, X.; Goodman, D. W. Onset of catalytic activity of gold clusters on titania with the appearance of nonmetallic properties. *Science*, **1998**, *281*, 1647–1650.

[21] Tada, H.; Mitsui, T.; Kiyonaga, T.; Akita, T.; Tanaka, K. All-solid-state Z-scheme in CdS–Au–TiO_2 three-component nanojunction system. *Nat. Mater.* **2006**, *5*, 782–786.

[22] Mokari, T.; Rothenberg, E.; Popov, I.; Costi, R.; Banin, U. Selective growth of metal tips onto semiconductor quantum rods and tetrapods. *Science* **2004**, *304*, 1787–1790.

[23] Elmalem, E.; Saunders, A. E.; Costi, R.; Salant, A.; Banin, U. Growth of photocatalytic CdSe–Pt nanorods and nanonets. *Adv. Mater.* **2008**, *20*, 4312–4317.

[24] Qian, H. S.; Antonietti, M.; Yu, S. H. Hybrid "golden fleece": Synthesis and catalytic performance of uniform carbon nanofibers and silica nanotubes embedded with a high population of noble-metal nanoparticles. *Adv. Funct. Mater.* **2007**, *17*, 637–643.

[25] Li, S.; Liu, G.; Lian H.; Jia, M.; Zhao, G.; Jiang, D.; Zhang, W. Low-temperature CO oxidation over supported Pt catalysts prepared by colloid-deposition method. *Catal. Commun.* **2008**, *9*, 1045–1049.

[26] Ko, E. Y.; Park, E. D.; Lee, H. C.; Lee, D.; Kim, S. Supported Pt–Co catalysts for selective CO oxidation in a hydrogen-rich stream. *Angew. Chem. Int. Ed.* **2007**, *46*, 734–737.

[27] Qian, K.; Sun, H.; Huang, W.; Fang, J.; Lv, S.; He, B.; Jiang, Z.; Wei, S. Restructuring-induced activity SiO_2-supported large Au nanoparticles in low-temperature CO oxidation. *Chem. Eur. J.* **2008**, *14*, 10595–10602.

[28] Qian, K.; Huang, W. X.; Jiang, Z.; Sun, H. Anchoring highly active gold nanoparticles on SiO_2 by CoO_x additive. *J. Catal.* **2007**, *248*, 137–141.

[29] Fujishima, A.; Honda, K. Electrochemical photolysis of water at a semiconductor electrode. *Nature* **1972**, *238*, 37–38.

[30] Cozzoli, P. D.; Comparelli, R.; Fanizza, E.; Curri, M. L.; Agostiano, A.; Laub, D. Photocatalytic synthesis of silver nanoparticles stabilized by TiO_2 nanorods: A semiconductor/metal nanocomposite in homogeneous nonpolar solution. *J. Am. Chem. Soc.* **2004**, *126*, 3868–3879.

[31] Chan, S. C.; Barteau, M. A. Preparation of highly uniform Ag/TiO_2 and Au/TiO_2 supported nanoparticle catalysts by photodeposition. *Langmuir* **2005**, *21*, 5588–5595.

[32] Ohtani, B.; Ogawa, Y.; Nishimoto, S. I. Photocatalytic activity of amorphous-anatase mixture of titanium(Ⅳ) oxide particles suspended in aqueous solutions. *J. Phys. Chem. B.* **1997**, *101*, 3746–3742.

[33] Pacholski, C.; Kornowski, A.; Weller, H. Site-specific photodeposition of silver on ZnO nanorods. *Angew. Chem. Int. Ed.* **2004**, *43*, 4774–4777.

[34] Dukovic, G.; Merkle, M. G.; Nelson, J. H.; Hughes, S. M.; Alivisatos, A. P. Photodeposition of Pt on colloidal CdS and CdSe/CdS semiconductor nanostructures. *Adv. Mater.* **2008**, *20*, 4306–4311.

[35] Lee, H.; Habas, S. E.; Kweskin, S.; Butcher, D.; Somorjai, G. A.; Yang, P. Morphological control of catalytically active

platinum nanocrystals. *Angew. Chem. Int. Ed.* **2006**, *45*, 7824–7828.

[36] Hosono, E.; Fujihara, S.; Kakiuchi, K.; Imai, H. Growth of submicrometer-scale rectangular parallelepiped rutile TiO_2 films in aqueous $TiCl_3$ solutions under hydrothermal conditions. *J. Am. Chem. Soc.* **2004**, *126*, 7790–7791.

[37] Wang, D.; Liu, J.; Huo, Q.; Nie, Z.; Lu, W.; Williford, R. E.; Jiang, Y. B. Surface-mediated growth of transparent, oriented, and well-defined nanocrystalline anatase titania films. *J. Am. Chem. Soc.* **2006**, *128*, 13670–13671.

[38] Swamy, V.; Muddle, B. C. Size-dependent modifications of the Raman spectrum of rutile TiO_2. *Appl. Phys. Lett.* **2006**, *89*, 163118.

[39] Wang, H. F.; Huff, T. B.; Zweifel, D. A.; He, W.; Low, P. S.; Wei, A.; Cheng, J. X. *In vitro* and *in vivo* two-photon luminescence imaging of single gold nanorods. *P. Natl. Acad. Sci. USA.* **2005**, *102*, 15752–15756.

[40] Atalic, B.; Üner, D. Structure sensitivity of selective CO oxidation over Pt/γ-Al_2O_3. *J. Catal.* **2006**, *241*, 268–275.

[41] Park, J. Y.; Zhang, Y.; Grass, M.; Zhang, T.; Somorjai, G. Tuning of catalytic CO oxidation by changing composition of Rh–Pt bimetallic nanoparticles. *Nano Lett.* **2008**, *8*, 673–677.

[42] İnce, T.; Uysal, G.; Akın, A. N.; Yıldırım, R. Selective low-temperature CO oxidation over Pt–Co–Ce/Al_2O_3 in hydrogen-rich streams. *Appl. Catal. A* **2005**, *292*, 171–176.

[43] Alayoglu, S.; Nilekar, A. U.; Mavrikakis, M.; Eichhorn, B. Ru–Pt core–shell nanoparticles for preferential oxidation of carbon monoxide in hydrogen. *Nat. Mater.* **2008**, *7*, 333–338.

[44] Behm, R. J.; Christmann, K.; Ertl, G.; Van Hove, M. A.; Thiel, P. A.; Weinberg, W. H. Structure of CO adsorbed on Pd (100)—LEED and HREELS analysis. *Surf. Sci.* **1979**, *88*, L59–L66.

[45] Son, W. K.; Youk, J. H.; Lee, T. S.; Park, W. H. Preparation of antimicrobial ultrafine cellulose acetate fibers with silver nanoparticles. *Macromol. Rapid Commun.* **2004**, *25*, 1632–1637.

[46] Wang Y. M.; Du, G. J.; Liu, H.; Liu, D.; Qin, S. B.; Wang, N.; Hu, C. G.; Tao, X. T.; Jiao, J.; Wang, J. Y.; Wang, Z. L. Nanostructured sheets of Ti–O nanobelts for gas sensing and antibacterial applications. *Adv. Funct. Mater.* **2008**, *18*, 1131–1137.

[47] Niňo-Martínez, N.; Martínez-Castaňón, G. A.; Aragón-Piňa, A.; Martínez-Gutierrez, F.; Martínez-Mendoza, J. R.; Ruiz, F. Characterization of silver nanoparticles synthesized on titanium dioxide fine particles. *Nanotechnology* **2008**, *19*, 065711.

[48] Rai, M.; Yadav, A.; Gade, A. Silver nanoparticles as a new generation of antimicrobials. *Biotechnol. Adv.* **2009**, *27*, 76–83.

[49] Zhang, H.; Chen, G. Potent antibacterial activities of Ag/TiO_2 nanocomposite powders synthesized by a one-pot sol–gel method. *Environ. Sci. Technol.* **2009**, *43*, 2905–2910.

[50] Hu, B.; Wang, S. B.; Wang, K.; Zhang, M.; Yu, S. H. Microwave-assisted rapid facile "green" synthesis of uniform silver nanoparticles: Self-assembly into multilayered films and their optical properties. *J. Phys. Chem. C* **2008**, *112*, 11169–11174.

[51] Priya, R.; Baiju, K. V.; Shukla, S.; Biju, S.; Reddy, M. L. P.; Patil, K.; Warrier, K. G. K. Comparing ultraviolet and chemical reduction techniques for enhancing photocatalytic activity of silver oxide/silver deposited nanocrystalline anatase titania. *J. Phys. Chem. C* **2009**, *113*, 6243–6255.

[52] Zhang, Y. X.; Li, G. H.; Jin, Y. X.; Zhang, Y.; Zhang, J.; Zhang, L. D. Hydrothermal synthesis and photoluminescence of TiO_2 nanowires. *Chem. Phys. Lett.* **2002**, *365*, 300–304.

[53] Wu, J. M.; Shih, H. C.; Wu, W. T. Formation and photoluminescence of single-crystalline rutile TiO_2 nanowires synthesized by thermal evaporation. *Nanotechnology* **2005**, *17*, 105–109.